Multidimensional encoding of restricted and anisotropic diffusion by double rotation of the *q*-vector

Hong Jiang[1], Leo Svenningsson[1], Daniel Topgaard[1]

[1]Physical Chemistry, Lund University, P.O. Box 124, SE-22100 Lund, Sweden

Correspondence to: Daniel Topgaard (daniel.topgaard@fkem1.lu.se)

Abstract. Diffusion NMR and MRI methods building on the classic pulsed gradient spin echo sequence are sensitive to many aspects of translational motion, including time/frequency-dependence ("restriction"), anisotropy, and flow, which leads to ambiguities when interpreting experimental data from complex heterogeneous materials such as living biological tissues. While the oscillating gradient technique specifically targets frequency-dependence and permits control of the sensitivity to flow, tensor-valued encoding enables investigations of anisotropy in orientationally disordered materials. Here we propose a simple scheme derived from the "double rotation" technique in solid-state NMR to generate a family of modulated gradient waveforms allowing for comprehensive exploration of the two-dimensional frequency-anisotropy space and convenient investigation of both restricted and anisotropic diffusion with a single multidimensional acquisition protocol, thereby combining the desirable characteristics of the oscillating gradient and tensor-valued encoding techniques. The method is demonstrated by measuring multicomponent isotropic Gaussian diffusion in simple liquids, anisotropic Gaussian diffusion in a polydomain lyotropic liquid crystal, and restricted diffusion in a yeast cell sediment.

1 Introduction

Magnetic field gradients applied during the dephasing and rephasing periods of a spin echo sequence (Hahn, 1950) render the NMR signal sensitive to various aspects of translational motion including bulk diffusivity (Douglass and McCall, 1958), flow (Carr and Purcell, 1954), time/frequency-dependence ("restriction") (Woessner, 1963), anisotropy (Boss and Stejskal, 1965), and exchange (Kärger, 1969). Although the conventional and ubiquitous pulsed gradient spin echo sequence by Stejskal and Tanner (1965) may give information about all of these aspects, more elaborate gradient modulations (Tanner, 1979; Cory et al., 1990; Callaghan and Manz, 1994; Mori and van Zijl, 1995) are required to unambiguously assign a certain mechanism to the experimental observations (Topgaard, 2017; Lundell and Lasič, 2020). Diffusion MRI methods incorporating such advanced diffusion encoding schemes have recently been shown to have potential for clinical research applications (Reymbaut et al., 2020)—some notable examples being oscillating gradients to estimate cell sizes (Xu et al., 2021) and tensor-valued encoding to characterize cell shapes (Daimiel Naranjo et al., 2021) in breast tumors.

The sensitivity of the MRI signal to the various types of motion can be quantified with the tensor-valued encoding spectrum $\mathbf{b}(\omega)$ (Topgaard, 2019a; Lundell and Lasič, 2020), the trace of which equals the dephasing power spectrum (Stepišnik, 1981)—relevant for isotropic restricted diffusion—and whose integral over ω equals the conventional b-matrix (Basser et al., 1994) giving information about diffusion anisotropy. While most studies focus on either the frequency-dependent (Aggarwal, 2020) or tensorial (Reymbaut, 2020) aspects of the encoding, Lundell et al. (2019) suggested joining them into a common multidimensional framework. The approach was demonstrated with gradient waveforms deriving from the magic-angle spinning (MAS) technique in solid-state NMR spectroscopy (Andrew et al., 1959; Eriksson et al., 2013; Topgaard, 2013), which, however, offer only limited access to the frequency and anisotropy dimensions.

Expanding on the results of Lundell et al. (2019), we here take inspiration from the "double rotation" (DOR) technique in solid-state NMR (Samoson et al., 1998) and derive a family of gradient waveforms for comprehensive exploration of, in particular, the frequency-anisotropy dimensions of $\mathbf{b}(\omega)$, as quantified by the centroid frequency ω_{cent} (Arbabi et al., 2020) and encoding anisotropy b_{Δ} (Eriksson et al., 2015), in addition to the b-value and b-vector (Θ,Φ) of conventional diffusion tensor imaging (Kingsley, 2006). While ω_{cent} is key for characterizing restricted diffusion (Stepišnik and Callaghan, 2000), the

variable b_Δ enables quantification of anisotropy in orientationally disordered materials (Eriksson et al., 2015) and estimation of nonparametric diffusion tensor distributions (de Almeida Martins and Topgaard, 2016; Topgaard, 2019b). The ability of the new gradient waveforms to give access to the complete 2D ω_{cent}-b_Δ plane is demonstrated by microimaging measurements on previously studied phantoms with well-defined restriction and anisotropy properties, namely water (Mills, 1973) and concentrated salt solution (Wadsö et al., 2009) with isotropic Gaussian diffusion, a lamellar liquid crystal giving anisotropic Gaussian diffusion (Topgaard, 2016), and a yeast cell sediment exhibiting isotropic restricted diffusion (Malmborg et al., 2006).

2 Theoretical background

To set the stage for later sections dealing with the proposed gradient waveforms to investigate both frequency-dependent and tensorial aspects of translational motion, we here include a brief summary of the relevant theory which can be found in greater detail in the textbooks by Price (2009) and Callaghan (2011), as well as in the comprehensive review by Lundell and Lasič (2020). Readers already familiar with the background material may proceed directly to the design of gradient waveforms in section 3 after noting Eqs. (32) and (34) with the definitions of the main variables ω_{cent} and b_Δ reporting on the sensitivity to restriction and anisotropy.

2.1 Encoding of translational motion by magnetic field gradients

Figure 1 illustrates the effects of a general gradient waveform $\mathbf{g}(t)$ on the NMR signal from an ensemble of spins undergoing restricted diffusion and flow within an infinite cylinder. As shown with the 2D and 3D plots of $\mathbf{g}(t)$ in Figure 1a, both the magnitude and direction of the gradient vector is changing smoothly with time. Simultaneously, the spins spread out and gradually drift from their initial positions (Figure 1b). The time-dependent normalized signal $E(t)$ is given by

$$E(t) = \langle \exp\left(\mathrm{i}\phi(t)\right) \rangle, \tag{1}$$

where $\langle \cdots \rangle$ denotes an ensemble mean and the time-dependent phase $\phi(t)$ of a single spin with gyromagnetic ratio γ is determined by the time integral of the scalar product between $\mathbf{g}(t)$ the time-dependent position $\mathbf{r}(t)$ according to

$$\phi(t) = -\gamma \int_0^t \mathbf{g}(t') \cdot \mathbf{r}(t') \mathrm{d}t'. \tag{2}$$

The interplay between $\mathbf{g}(t)$ and $\mathbf{r}(t)$ results in $\phi(t)$ evolving from zero for all spins at $t = 0$ to periodic patterns with varying directions and spatial wavelengths at intermediate times and, finally, an overall phase shift superposed on partially randomized values. From Eq. (1) follows that the latter phase dispersion leads to a decrease in the magnitude of the signal.

The evolution of $\phi(t)$ may be rationalized by partial integration of Eq. (2) into

$$\phi(t) = -\mathbf{q}(t) \cdot \mathbf{r}(t) + \int_0^t \mathbf{q}(t') \cdot \mathbf{v}(t') \mathrm{d}t', \tag{3}$$

where $\mathbf{q}(t)$ is the dephasing vector, defined as

$$\mathbf{q}(t) = \gamma \int_0^t \mathbf{g}(t') \mathrm{d}t', \tag{4}$$

and $\mathbf{v}(t) = \mathrm{d}\mathbf{r}(t)/\mathrm{d}t$ is the time-dependent velocity. The spatial periodicity in $\phi(t)$ at intermediate times is according to the first term in Eq. (3) given by the scalar product between $\mathbf{q}(t)$ and $\mathbf{r}(t)$, which is utilized to obtain spatial resolution in MRI where the dephasing vector is usually denoted $\mathbf{k}(t)$. The plots of $\mathbf{q}(t)$ in Figure 1a show smooth changes of both the magnitude and direction of the vector with time.

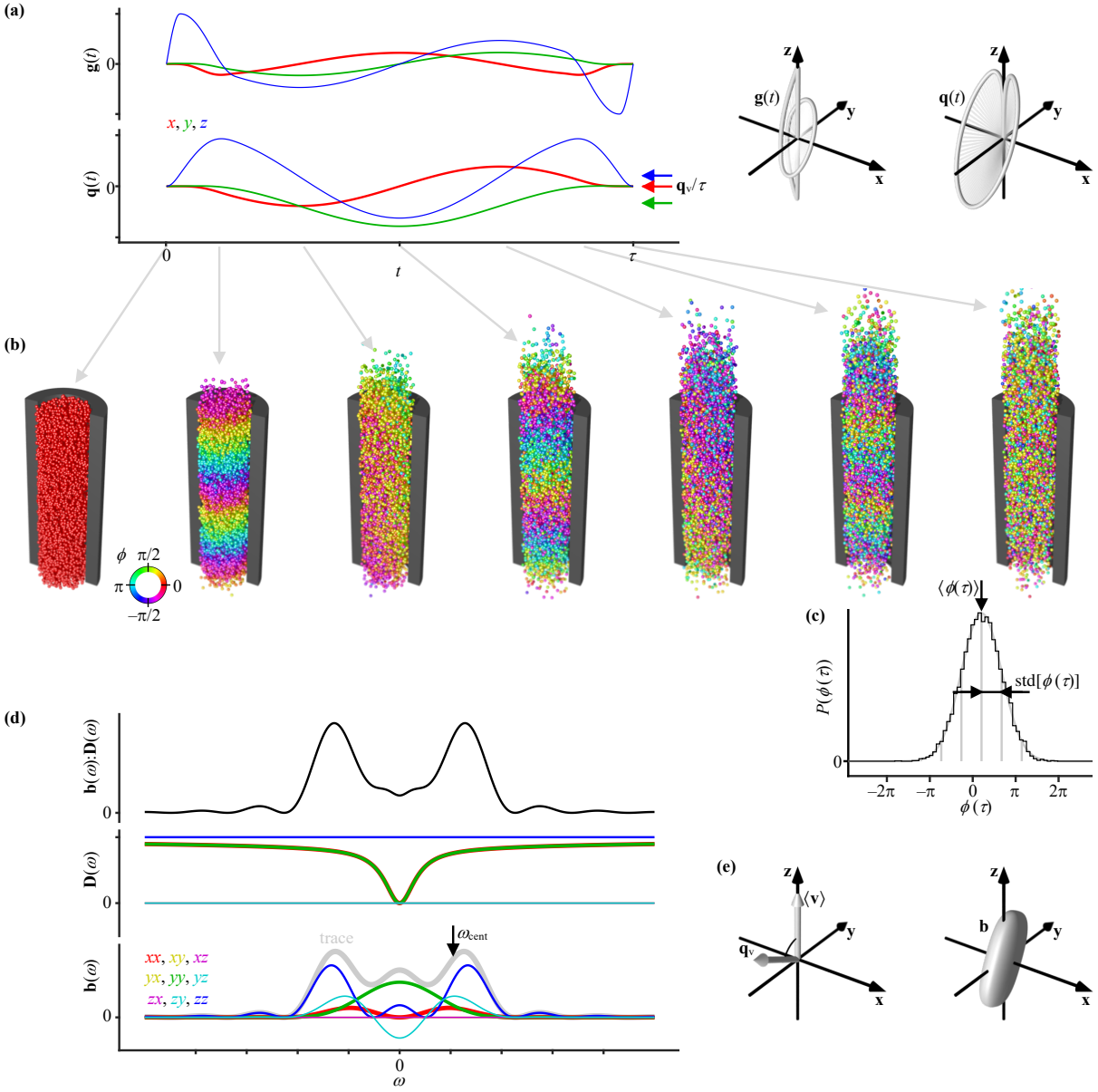

Figure 1. Principles of motion encoding by general gradient waveforms. **(a)** Time-dependent gradient $\mathbf{g}(t)$ and dephasing vector $\mathbf{q}(t)$ illustrated as 2D graphs of Cartesian components vs. t (left) and 3D plots of trajectories through space (right). The average values of the $\mathbf{q}(t)$ components within the time interval from $t = 0$ to τ are indicated with arrows labeled $\mathbf{q}_v/\tau$, where the velocity-encoding vector $\mathbf{q}_v$ is defined in Eq. (15). **(b)** Sequence of snapshots from a random walk simulation of an ensemble of spins (spheres) undergoing restricted diffusion and flow within an infinite cylinder (black section) during application of the waveforms in panel (a). Each spin is color-coded with its time-dependent phase $\phi(t)$ given by the interplay between $\mathbf{g}(t)$ and the spin positions $\mathbf{r}(t)$ according to Eq. (2). **(c)** Phase distribution $P(\phi(\tau))$ for the ensemble of spins at $t = \tau$ (black histogram) and a Gaussian (grey smooth line) with mean $\langle\phi(\tau)\rangle$ and standard deviation std$[\phi(\tau)]$ (spacing between grey vertical lines) which give the phase shift α and attenuation factor β of the signal $E(\tau)$ via Eqs. (8), (9), and (11). **(d)** Frequency-dependent elements (color coded) of the tensor-valued encoding spectrum $\mathbf{b}(\omega)$ and diffusion spectrum $\mathbf{D}(\omega)$, as well as their tensor dot product $\mathbf{b}(\omega)$:$\mathbf{D}(\omega)$ which gives β via Eq. (21). The centroid frequency ω_{cent} (arrow) is obtained from the trace of $\mathbf{b}(\omega)$ (gray line) through Eq. (32). **(e)** 3D plots of the ensemble mean velocity $\langle\mathbf{v}\rangle$, velocity-encoding vector $\mathbf{q}_v$, and encoding tensor $\mathbf{b}$, the latter being defined in Eq. (33). The scalar product of $\langle\mathbf{v}\rangle$ and $\mathbf{q}_v$ gives α by Eq. (14).

Focusing on translational displacements rather than absolute positions, we select a time τ where

$$\mathbf{q}(\tau) = 0 \tag{5}$$

and the first term in Eq. (3) vanishes while the second one remains:

$$\phi(\tau) = \int_0^\tau \mathbf{q}(t) \cdot \mathbf{v}(t)\mathrm{d}t. \tag{6}$$

The value of $\phi(\tau)$ in Eq. (6) is insensitive to $\mathbf{r}(\tau)$ but depends on the history of $\mathbf{q}(t)$ and $\mathbf{v}(t)$ in the interval from $t = 0$ to τ.

2.2 Gaussian phase distribution approximation

As shown in Figure 1c, the selected gradient waveform and random walk simulation parameters yield a phase distribution $P(\phi(t))$ that at $t = \tau$ is well approximated as a Gaussian function with mean $\langle\phi(\tau)\rangle$ and standard deviation $\mathrm{std}[\phi(\tau)] = (\langle\phi(\tau)^2\rangle - \langle\phi(\tau)\rangle^2)^{1/2}$. The Gaussian function can be expressed as

$$P\big(\phi(\tau)\big) = \frac{1}{2\sqrt{\pi\beta}} \exp\left(-\frac{(\phi(\tau)-\alpha)^2}{4\beta}\right), \tag{7}$$

where

$$\alpha = \langle\phi(\tau)\rangle \tag{8}$$

and

$$\beta = \frac{1}{2}\big(\langle\phi(\tau)^2\rangle - \langle\phi(\tau)\rangle^2\big). \tag{9}$$

After rewriting Eq. (1) as an integral,

$$E(\tau) = \int_{-\infty}^{\infty} P\big(\phi(\tau)\big)\exp\big(\mathrm{i}\phi(\tau)\big)\mathrm{d}\phi(\tau), \tag{10}$$

insertion of Eq. (7) may be evaluated to

$$E(\tau) = \exp(\mathrm{i}\alpha - \beta), \tag{11}$$

where α and β can be identified as quantitative measures of the overall phase shift and attenuation of the signal as previously deduced from visual inspection of the phases of the spin ensemble in Figure 1b. The Gaussian phase distribution approximation has been applied for the cases of free (Carr and Purcell, 1954; Douglass and McCall, 1958) and restricted diffusion (Neuman, 1974), and investigations of its ranges of validity can be found in the literature (Balinov et al., 1993; Stepišnik, 1999).

2.3 Mean velocity and velocity correlation function

Insertion of Eq. (6) into Eq. (8) yields

$$\alpha = \langle \int_0^\tau \mathbf{q}(t) \cdot \mathbf{v}(t)\mathrm{d}t\rangle, \tag{12}$$

which by separating $\mathbf{v}(t)$ into the ensemble mean $\langle\mathbf{v}(t)\rangle = \langle\mathbf{v}\rangle$ and fluctuating part $\mathbf{u}(t)$, defined by

$$\mathbf{u}(t) = \mathbf{v}(t) - \langle\mathbf{v}\rangle, \tag{13}$$

can be evaluated to

$$\alpha = \mathbf{q}_\mathrm{v} \cdot \langle \mathbf{v} \rangle, \tag{14}$$

where the flow encoding vector $\mathbf{q}_\mathrm{v}$ is defined as

$$\mathbf{q}_\mathrm{v} = \int_0^\tau \mathbf{q}(t)\mathrm{d}t. \tag{15}$$

Correspondingly, insertion of Eq. (6) into Eq. (9) gives

$$\beta = \frac{1}{2}\left(\langle \left[\int_0^\tau \mathbf{q}(t) \cdot \mathbf{v}(t)\mathrm{d}t \right]^2 \rangle - \langle \int_0^\tau \mathbf{q}(t) \cdot \mathbf{v}(t)\mathrm{d}t \rangle^2 \right), \tag{16}$$

which by reordering the time integrals and ensemble means, as well as noting that $\langle \mathbf{u}(t) \cdot \langle \mathbf{v} \rangle \rangle = 0$, can be expressed as

$$\beta = \int_0^\tau \int_0^t \mathbf{q}(t)^\mathrm{T} \cdot \langle \mathbf{u}(t)\mathbf{u}(t')^\mathrm{T} \rangle \cdot \mathbf{q}(t')\mathrm{d}t\, \mathrm{d}t', \tag{17}$$

where $\langle \mathbf{u}(t)\mathbf{u}(t')^\mathrm{T} \rangle$ is the tensor-valued velocity correlation function.

2.4 Transformation to the frequency domain

After introducing the dephasing spectrum $\mathbf{q}(\omega)$ and diffusion spectrum $\mathbf{D}(\omega)$ by Fourier transformations to the frequency (ω) domain according to

$$\mathbf{q}(\omega) = \int_0^\tau \mathbf{q}(t) \exp(\mathrm{i}\omega t)\, \mathrm{d}t \tag{18}$$

and

$$\mathbf{D}(\omega) = \frac{1}{2}\int_{-\infty}^{\infty} \langle \mathbf{u}(t)\mathbf{u}(t')^\mathrm{T} \rangle \exp(\mathrm{i}\omega(t'-t))\, \mathrm{d}(t'-t), \tag{19}$$

Eq. (17) can be recast into

$$\beta = \frac{1}{2\pi}\int_{-\infty}^{\infty} \mathbf{q}(\omega)^\mathrm{T} \cdot \mathbf{D}(\omega) \cdot \mathbf{q}(-\omega)\mathrm{d}\omega, \tag{20}$$

which can be expressed more compactly as

$$\beta = \int_{-\infty}^{\infty} \mathbf{b}(\omega) \colon \mathbf{D}(\omega)\mathrm{d}\omega, \tag{21}$$

where $\mathbf{b}(\omega)$ is the tensor-valued encoding spectrum defined by (Topgaard, 2019a; Lundell and Lasič, 2020)

$$\mathbf{b}(\omega) = \frac{1}{2\pi}\mathbf{q}(\omega)\mathbf{q}(-\omega)^\mathrm{T} \tag{22}$$

and ":" denotes a tensor dot product (Basser et al., 1994):

$$\mathbf{b}(\omega) \colon \mathbf{D}(\omega) = \sum\nolimits_i \sum\nolimits_j b_{ij}(\omega) D_{ij}(\omega)\,. \tag{23}$$

Combining Eqs. (11), (14), and (21) yields

$$E(\tau) = \exp\left(\mathrm{i}\mathbf{q}_\mathrm{v} \cdot \langle \mathbf{v} \rangle - \int_{-\infty}^{\infty} \mathbf{b}(\omega) \colon \mathbf{D}(\omega)\mathrm{d}\omega \right), \tag{24}$$

where the motion-encoding properties of $\mathbf{g}(t)$ are summarized in $\mathbf{q}_v$ and $\mathbf{b}(\omega)$ as illustrated in Figure 1d and e. While $\mathbf{q}_v$ and $\langle \mathbf{v} \rangle$ are (ω-independent) vectors, both $\mathbf{b}(\omega)$ and $\mathbf{D}(\omega)$ are symmetric second-order tensors at each value of ω.

2.5 Diffusion spectra for some simple cases

For a liquid with bulk diffusivity D_0 confined in d dimensions in planar ($d = 1$), cylindrical ($d = 2$), or spherical ($d = 3$) compartments with radius r, the diffusion spectrum $D_{\text{rest}}(\omega)$ in the restricted dimensions can be expressed as (Stepišnik, 1993)

$$D_{\text{rest}}(\omega) = D_0 - \sum_k w_k \frac{D_0 - D_\infty}{1 + \omega^2/\Gamma_k^2}, \tag{25}$$

where

$$\Gamma_k = \frac{\xi_k^2 D_0}{r^2} \tag{26}$$

and

$$w_k = \frac{2}{\xi_k^2 + 1 - d}. \tag{27}$$

Eq. (25) includes the long-range diffusivity D_∞, allowing for finite permeability of the compartment walls (Lasič et al., 2009), and can be recognized as a sum of Lorentzians with widths Γ_k and weights w_k. In Eqs. (26) and (27), ξ_k is the kth solution of

$$\xi J_{d/2-1}(\xi) - (d-1) J_{d/2}(\xi) = 0, \tag{28}$$

where J_ν is the νth order Bessel function of the first kind. Taking the cylindrical case in Figure 1b as an example, the tensor-valued diffusion spectrum $\mathbf{D}(\omega)$ is given by

$$\mathbf{D}(\omega) = \mathbf{R}(\theta, \phi) \begin{pmatrix} D_{\text{rest}}(\omega) & 0 & 0 \\ 0 & D_{\text{rest}}(\omega) & 0 \\ 0 & 0 & D_0 \end{pmatrix} \mathbf{R}^{-1}(\theta, \phi) \tag{29}$$

where θ and ϕ are polar and azimuthal angles, giving the orientation of the cylinder in the lab frame, and $\mathbf{R}(\theta,\phi)$ is a rotation matrix. Figure 1d includes a plot of $\mathbf{D}(\omega)$ for the case $\theta = 0$ and $\phi = 0$ where all off-diagonal elements are zero. At high values of ω, the diagonal elements converge towards D_0 corresponding to isotropic diffusion. Conversely, the effects of anisotropy reaches a maximum in the low-ω limit where $D_{\text{rest}}(\omega)$ approaches D_∞ which in the example in Figure 1d equals zero. The planar version of Eq. (29) is obtained by exchanging $D_{\text{rest}}(\omega)$ and D_0. In the low-ω limit, the planar and cylindrical cases are often combined into a single expression

$$\mathbf{D} = \mathbf{R}(\theta, \phi) \begin{pmatrix} D_\perp & 0 & 0 \\ 0 & D_\perp & 0 \\ 0 & 0 & D_\parallel \end{pmatrix} \mathbf{R}^{-1}(\theta, \phi), \tag{30}$$

where $D_\parallel$ and $D_\perp$ are the eigenvalues parallel and perpendicular to the main symmetry axis of the compartment. For completeness, we note that $D_{\text{rest}}(\omega)$ and $\mathbf{D}$ in Eqs. (25) and (30) reduce to an ω-independent scalar diffusion coefficient D for the special case of isotropic Gaussian diffusion where $D = D_0 = D_\infty = D_\perp = D_\parallel$.

2.6 Key properties of the tensor-valued diffusion encoding spectrum

While the signal expression in Eq. (24) takes the ω-dependence and tensorial properties of both $\mathbf{b}(\omega)$ and $\mathbf{D}(\omega)$ into account, and may be numerically evaluated as a single matrix multiplication after discretization in the ω-dimension and appropriate reordering of the tensor elements, the common occurrence of systems exhibiting approximately Gaussian (ω-independent) and/or isotropic diffusion has led to the introduction of simplified descriptions focusing on some specific aspects. In the

absence of diffusion anisotropy—which is obviously not the case for the example in Figure 1—it is sufficient to use the dephasing power spectrum $b(\omega)$ (Stepišnik, 1981) obtained from $\mathbf{b}(\omega)$ by

$$b(\omega) = \mathrm{trace}\{\mathbf{b}(\omega)\}. \tag{31}$$

The sensitivity to restriction can be summarized by the centroid frequency ω_{cent} (Arbabi et al., 2020) defined as

$$\omega_{\mathrm{cent}} = \frac{1}{b}\int_{-\infty}^{\infty} |\omega| b(\omega) \mathrm{d}\omega. \tag{32}$$

In addition to all the tensor elements of $\mathbf{b}(\omega)$, Figure 1d includes a plot of $b(\omega)$ with an arrow indicating ω_{cent}. The example of $b(\omega)$ covers both low- and high-ω features of $\mathbf{D}(\omega)$ and is thus less well suited for exploring ω-dependent diffusion processes than gradient modulation schemes comprising trains of rectangular pulses (Callaghan and Stepišnik, 1995), multiple smooth oscillations (Parsons et al., 2003), or a CPMG sequence in the presence of a constant gradient (Lasič et al., 2006), where the encoding power is concentrated in a narrow frequency range and the single value ω_{cent} captures most of the relevant information about the spectral content. Even when the peaks in $b(\omega)$ are broader than the features in $\mathbf{D}(\omega)$, the ω_{cent} metric has some value as a book keeping tool but is less suitable for quantitative analysis.

For anisotropic systems with Gaussian diffusion, it is useful to introduce the b-matrix $\mathbf{b}$ (Basser et al., 1994) by

$$\mathbf{b} = \int_{-\infty}^{\infty} \mathbf{b}(\omega) \mathrm{d}\omega. \tag{33}$$

The sensitivity to anisotropy is given by the "shape" of the tensor which can be quantified with the encoding anisotropy b_Δ and asymmetry b_η (Eriksson et al., 2015) defined as

$$b_\Delta = \frac{1}{b}\left(b_{ZZ} - \frac{b_{YY} + b_{XX}}{2}\right) \tag{34}$$

and

$$b_\eta = \frac{3}{2}\frac{b_{YY} - b_{XX}}{b b_\Delta}, \tag{35}$$

where b_{XX}, b_{YY}, and b_{ZZ} are the eigenvalues of $\mathbf{b}$ ordered according to the Haeberlen convention $|b_{ZZ} - b/3| > |b_{XX} - b/3| > |b_{YY} - b/3|$ (Haeberlen, 1976) and

$$b = \mathrm{trace}\{\mathbf{b}\} \tag{36}$$

is the conventional b-value (Le Bihan et al., 1986) that gives the overall magnitude of the diffusion encoding. Figure 1e shows a superquadric tensor glyph (Kindlmann, 2004) representation of $\mathbf{b}$ where all eigenvalues and both shape parameters b_Δ and b_η are non-zero.

From the definitions of $\mathbf{q}_\mathrm{v}$, $\mathbf{q}(\omega)$, and $\mathbf{b}(\omega)$ in Eqs. (15), (18), and (22) follow that the $\omega = 0$ values of $\mathbf{b}(\omega)$ are proportional to $\mathbf{q}_\mathrm{v}\mathbf{q}_\mathrm{v}^\mathrm{T}$ and thus report on the sensitivity to flow, albeit with some ambiguity with respect to the directionality: the vectors $\mathbf{q}_\mathrm{v}$ and $-\mathbf{q}_\mathrm{v}$ give the same $\mathbf{b}(\omega = 0)$. It should be noted that $\mathbf{q}_\mathrm{v}$ is not necessarily colinear with any of the eigenvectors of $\mathbf{b}$.

2.7 Special cases for data analysis

For data fitting purposes, it is convenient to write the normalized signal E as the ratio

$$E = S/S_0, \tag{37}$$

where S is detected signal and S_0 the signal obtained in a reference measurement with the amplitudes of the motion-encoding gradients set to zero. Then Eq (24) can be expressed as

$$S = S_0 \exp\left(i\mathbf{q}_v \cdot \langle \mathbf{v} \rangle - \int_{-\infty}^{\infty} \mathbf{b}(\omega) : \mathbf{D}(\omega) d\omega \right). \quad (38)$$

For the special cases of (i) isotropic restricted, (ii) anisotropic Gaussian, and (iii) isotropic Gaussian diffusion in the absence of net flow ($\langle \mathbf{v} \rangle = 0$), Eq (38) is simplified to

$$S = S_0 \exp\left(- \int_{-\infty}^{\infty} b(\omega) D(\omega) d\omega \right), \quad (39)$$

$$S = S_0 \exp(-\mathbf{b} : \mathbf{D}), \quad (40)$$

and

$$S = S_0 \exp(-bD), \quad (41)$$

respectively, where $D(\omega)$ is the (isotropic) diffusion spectrum, $\mathbf{D}$ the (ω-independent) diffusion tensor, and D the (isotropic and ω-independent) diffusion coefficient introduced in section 2.5 above.

For a heterogeneous system including multiple sub-ensembles i with individual signals S_i, each of which given by one of Eqs. (38)-(41) above, the total signal S is obtained by the sum

$$S = \sum_i S_i. \quad (42)$$

An important type of heterogeneity refers to the orientations of anisotropic objects with the extreme case of completely random orientations as in a "powder". In the special case of axial symmetry of both $\mathbf{b}$ and $\mathbf{D}$, powder averaging of Eq. (40) yields (Eriksson et al., 2015)

$$S = S_0 \exp(-bD_{iso}) \frac{\sqrt{\pi}}{2} \frac{\exp(A/3)}{\sqrt{A}} \mathrm{erf}\left(\sqrt{A} \right) \quad (43)$$

where

$$A = 3bD_{iso} b_\Delta D_\Delta. \quad (44)$$

In Eq. (44), D_{iso} is the isotropic diffusivity and D_Δ the normalized diffusion anisotropy defined as

$$D_{iso} = \frac{1}{3} \mathrm{trace}\{\mathbf{D}\} = \frac{D_\parallel + 2D_\perp}{3} \quad (45)$$

and

$$D_\Delta = \frac{D_\parallel - D_\perp}{3D_{iso}}, \quad (46)$$

where $D_\parallel$ and $D_\perp$ were introduced in Eq. (30). The definitions of b and b_Δ can be found in Eqs. (34) and (36).

3 Design of gradient waveforms by double rotation of the q-vector

Expanding on previous magic-angle spinning (Andrew et al., 1959; Eriksson et al., 2013; Topgaard, 2013) and variable-angle spinning (Frydman et al., 1992; Topgaard, 2016, 2017) approaches for generating motion-encoding gradient waveforms, we here apply the double rotation (DOR) technique (Samoson et al., 1998; Topgaard, 2019a) to probe the 2D acquisition space spanned by the variables ω_{cent} and b_Δ defined in Eqs. (32) and (34). The q-vector trajectory $\mathbf{q}(t)$ is expressed in terms of its time-dependent magnitude $q(t)$ and unit vector $\mathbf{u}(t)$ as

$$\mathbf{q}(t) = q(t)\mathbf{u}(t). \tag{47}$$

For the special case of DOR, the unit vector is written as

$$\mathbf{u}(t) = \mathbf{R}_z\big(\psi_2(t)\big)\mathbf{R}_y(\zeta_2)\mathbf{R}_z\big(\psi_1(t)\big)\mathbf{R}_y(\zeta_1)[0 \quad 0 \quad 1]^{\mathrm{T}}, \tag{48}$$

where $\mathbf{R}_z$ and $\mathbf{R}_y$ are Euler rotation matrices, ζ_1 and ζ_2 are the inclinations of the two rotation axes, and $\psi_1(t)$ and $\psi_2(t)$ are the time-dependent angles of rotation. The rotations in Eq. (48) are applied from right to left and follow a *Z*-*Y* active rotation matrix convention.

Starting from a conventional one-dimensional gradient waveform $g_{1D}(t)$–for instance a pair of rectangular or sine-bell pulses of opposite polarity–the time-dependent functions $q(t)$ and $\psi_2(t)$ are given by (Topgaard, 2016)

$$q(t) = \gamma \int_0^t g_{1D}(t')\mathrm{d}t' \tag{49}$$

and

$$\psi_2(t) = \frac{\Delta\psi_2}{b} \int_0^t q^2(t')\mathrm{d}t', \tag{50}$$

where $\Delta\psi_2$ is the total angle of rotation during the encoding interval from time $t = 0$ to τ and

$$b = \int_0^\tau q^2(t)\mathrm{d}t \tag{51}$$

is the conventional *b*-value. After some exercises in trigonometry, combination of Eqs. (47)-(51) and the relation between $\mathbf{g}(t)$ and $\mathbf{q}(t)$ in Eq. (4) yields

$$\begin{aligned}\mathbf{g}_{\mathrm{DOR}}(t) = g_{1D}(t)&\begin{pmatrix} a_+\cos\psi_+(t) + a_-\cos\psi_-(t) + a_2\cos\psi_2(t) \\ a_+\sin\psi_+(t) - a_-\sin\psi_-(t) + a_2\sin\psi_2(t) \\ a_0 - a_1\cos\psi_1(t) \end{pmatrix} \\ + g_{\mathrm{rot}}(t)&\begin{pmatrix} -(n+1)a_+\sin\psi_+(t) - (n-1)a_-\sin\psi_-(t) - a_2\sin\psi_2(t) \\ (n+1)a_+\cos\psi_+(t) - (n-1)a_-\cos\psi_-(t) + a_2\cos\psi_2(t) \\ na_1\sin\psi_1(t) \end{pmatrix},\end{aligned} \tag{52}$$

where

$$g_{\mathrm{rot}}(t) = \frac{\Delta\psi_2 q(t)^3}{\gamma b} \tag{53}$$

is the time-dependent magnitude of the rotating gradient vector,

$$\begin{aligned}\psi_1(t) &= n\psi_2(t) \\ \psi_\pm(t) &= (n \pm 1)\psi_2(t)\end{aligned} \tag{54}$$

are time-dependent rotation angles, and

$$\begin{aligned}a_0 &= \cos\zeta_1\cos\zeta_2 \\ a_1 &= \sin\zeta_1\sin\zeta_2 \\ a_2 &= \cos\zeta_1\sin\zeta_2 \\ a_\pm &= \sin\zeta_1\frac{\cos\zeta_2 \pm 1}{2}\end{aligned} \tag{55}$$

are amplitudes of the oscillating terms.

In the solid-state NMR field, DOR is applied with the inclinations $\zeta_1 = 54.7°$ and $\zeta_2 = 30.6°$, corresponding to zeros of the second and fourth Legendre polynomial, to eliminate both first and second order quadrupolar broadening of the NMR spectra of nuclei such as ^{23}Na (Samoson et al., 1998). While the encoding anisotropy b_Δ in Eq. (34) is closely related to the second Legendre polynomial (Eriksson et al., 2015), we are not yet aware of any diffusion analog of the quadrupolar interactions involving the fourth Legendre polynomial. Instead, we found that DOR with the inclinations $\zeta_1 = 90°$ and $\zeta_2 = -54.7°$ yields desirable properties for diffusion encoding, namely spectral content concentrated to a narrow frequency window for all of the elements of $\mathbf{b}(\omega)$. For $n > 1$ and the special case of $g_{1D}(t) \propto [\delta(t) - \delta(t-\tau)]$, where $\delta(x)$ is the Dirac delta function, these angles yield an isotropic b-tensor, corresponding to $b_\Delta = 0$. Waveforms for any values of b_Δ and b_η are then conveniently obtained by scaling the components of $\mathbf{g}_{DOR}(t)$ according to

$$\mathbf{g}(t) = \begin{bmatrix} g_X(t) \\ g_Y(t) \\ g_Z(t) \end{bmatrix} = \begin{bmatrix} g_{DOR,X}(t)\sqrt{1 - b_\Delta(1 + b_\eta)} \\ g_{DOR,Y}(t)\sqrt{1 - b_\Delta(1 - b_\eta)} \\ g_{DOR,Z}(t)\sqrt{1 + 2b_\Delta} \end{bmatrix}. \tag{56}$$

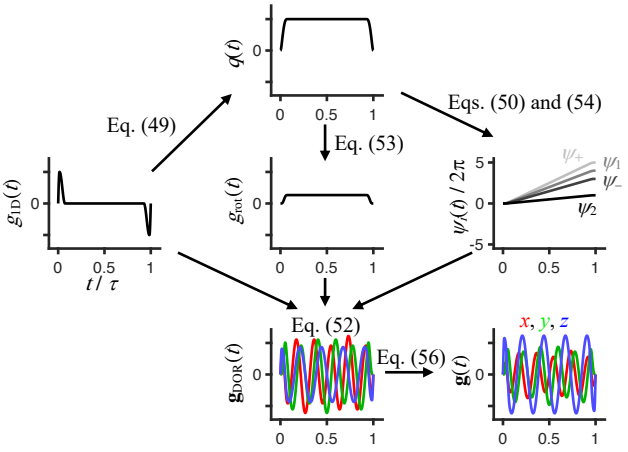

Figure 2. Flowchart for calculating a double-rotation gradient waveform $\mathbf{g}_{DOR}(t)$ given a one-dimensional dephasing/rephasing waveform $g_{1D}(t)$, rotation axis inclinations ζ_1 and ζ_2, double rotation ratio n, and total angle of rotation $\Delta\psi_2$ during the waveform duration τ. The waveform $g_{1D}(t)$, containing dephasing and rephasing pulses with sinusoidal ramps of durations ε_{up} and ε_{down}, gives the time-dependent magnitude of the dephasing vector $q(t)$ by Eq. (49), which yields the time-dependent rotation angles $\psi_i(t)$ via Eqs. (50) and (54) as well as the time-dependent magnitude of the rotating/oscillating gradient $g_{rot}(t)$ through Eq. (53). Combining $g_{1D}(t)$, $g_{rot}(t)$, and $\psi_i(t)$ via Eq. (52) gives $\mathbf{g}_{DOR}(t)$, which if $\zeta_1 = 90°$ and $\zeta_2 = -54.7°$, n is an integer above 1, and $\Delta\psi_2$ is a multiple of 2π achieves isotropic encoding tensors $\mathbf{b}$ where the anisotropy b_Δ and asymmetry b_η are both equal to zero. Finally, waveforms $\mathbf{g}(t)$ for any values of b_Δ and b_η are obtained by scaling of the Cartesian components of $\mathbf{g}_{DOR}(t)$ according to Eq. (56). The shown example was generated with the accompanying Matlab code (see supporting information) using $\varepsilon_{up} = 0.015\,\tau$, $\varepsilon_{down} = 0.06\,\tau$, $\Delta\psi_2 = 2\pi$, $n = 4$, $b_\Delta = 0.5$, and $b_\eta = 0.25$.

At the selected inclinations, the a_0 and a_2 terms in Eq. (52) equal zero while the remaining amplitudes evaluate to $a_1 \approx -0.816$, $a_+ \approx 0.789$, and $a_- \approx -0.211$. For the special case $g_{1D}(t) \propto [\delta(t) - \delta(t-\tau)]$, the main frequency components of $\mathbf{b}(\omega)$ are thus given by

$$\begin{aligned} \omega_\pm &= \frac{\psi_\pm(\tau)}{\tau} = (n \pm 1)\frac{\Delta\psi_2}{\tau} \text{ and} \\ \omega_1 &= \frac{\psi_1(\tau)}{\tau} = n\frac{\Delta\psi_2}{\tau}, \end{aligned} \tag{57}$$

where, according to Eq. (52), $\omega_{\pm}$ and ω_{I} are cleanly separated into the X,Y and Z directions, respectively. The mean frequency content, as quantified by the centroid frequency ω_{cent} defined in Eq. (32), can be estimated by weighting the contributions from the main frequency components with the corresponding amplitudes Eq. (52), but is more accurately calculated by numerical evaluation of Eq. (32) which also takes the finite durations of the sinusoidal oscillations into account. For rough prediction of ω_{cent} it is useful to note that $a_{+}^{2} >> a_{-}^{2}$, implying that the ω_{+}-component will dominate the spectra in the X,Y-directions. The scaling of the waveforms according to Eq. (56) preserves the frequency content in each of the eigendirections of the b-tensor, but shifts the value of ω_{cent} between the approximate extremes ω_{+} and ω_{I} for $b_{\Delta} = -1/2$ and 1, respectively. The differences in $\omega_{\pm}$ and ω_{I} may give rise to a directional dependence of the sensitivity to restriction as investigated for the $b_{\Delta} = 0$ case by de Swiet and Mitra (1996).

Figure 2 illustrates the series of calculations required to convert a conventional 1D waveform $g_{1\mathrm{D}}(t)$ and given values of ζ_1, ζ_2, $\Delta\psi_2$, n, b_{Δ}, and b_{η} to a 3D waveform $\mathbf{g}(t)$ by numerical evaluation of Eqs. (49)-(56). Following previous works to generate families of smooth gradient waveforms to explore the b_{Δ} and b_{η} dimensions of diffusion encoding (Topgaard, 2016, 2017), we here construct $g_{1\mathrm{D}}(t)$ from a dephasing lobe with quarter-sine ramp up of duration $\varepsilon_{\mathrm{up}}$ and half-cosine ramp down of duration $\varepsilon_{\mathrm{down}}$, as well as a rephasing lobe obtained by inversion and time-reversal of the dephasing one. The corresponding Matlab code is provided in the supporting information.

Figure 3 compiles waveforms and encoding spectra for an array of n and b_{Δ} at constant $g_{1\mathrm{D}}(t)$, τ, and $\Delta\psi_2$, yielding constant b. Increasing n leads to larger rotation angles $\psi_{\mathrm{I}}(t)$ and $\psi_{\pm}(t)$ and frequencies ω_{I} and $\omega_{\pm}$ according to Eqs. (54) and (57), respectively, at the expense of overall higher gradient amplitudes on account of the terms including n in Eq. (52). For most waveforms, vanishing values of $\mathbf{b}(\omega)$ at $\omega = 0$ correspond to $\mathbf{q}_{\mathrm{v}} = 0$ and insensitivity to flow. Many of the examples in Figure 3 are familiar from the literature, for instance conventional Stejskal-Tanner encoding at ($n = 0$, $b_{\Delta} = 1$), basic flow-compensated encoding (Caprihan and Fukushima, 1990) at ($n = 1$, $b_{\Delta} = 1$), and magic-angle spinning of the q-vector (Eriksson et al., 2013) at ($n = 0$, $b_{\Delta} = 0$). The series of $b_{\Delta} = 1$ and $-1/2$ waveforms with varying n resemble, respectively, the cosine-modulated oscillating gradients of Parsons et al. (2003) and the circularly polarized version introduced by Lundell et al. (2015). Correspondingly, the series of waveforms with $n = 0$ and varying b_{Δ} has previously been introduced as a diffusion version of the variable-angle spinning technique to correlate isotropic and anisotropic chemical shifts in solid-state NMR (Topgaard, 2016, 2017). The approach for joint investigation of restricted and anisotropic diffusion proposed by Lundell et al. (2019), combining isotropic encoding with "tuned" and "detuned" directional encodings, can be recognized as measurements at the three discrete points ($n = 0$, $b_{\Delta} = 0$), ($n = 0$, $b_{\Delta} = 1$), and ($n = 1$, $b_{\Delta} = 1$) of the 2D plane in Figure 3. For completeness, we note that the elliptically polarized oscillating gradients by Nielsen et al. (2018) can be reproduced with $b_{\Delta} = -1/2$ and b_{η} in the range from 0 to 3 (not included in Figure 3).

4 Proof-of-principle experiments

Magnesium nitrate hexahydrate, cobalt nitrate hexahydrate, and 1-decanol were purchased from Sigma-Aldrich Sweden AB and sodium octanoate from J&K Scientific via Th.Geyer in Sweden. Water was purified with a Milli-Q system. A sample with two-component isotropic diffusion was prepared by inserting a 4 mm NMR tube containing an aqueous solution saturated with magnesium nitrate (Wadsö et al., 2009) into a 10 mm NMR tube with water (Mills, 1973). The magnesium nitrate solution was spiked with a small amount cobalt nitrate (0.27 wt% saturated solution) to reduce T_1 and T_2 to approx. 500 and 50 ms, respectively. An anisotropic sample was prepared by mixing 85.79 wt% Milli-Q, 9.17 wt% 1-decanol, and 5.04 wt% sodium octanoate giving a lamellar liquid crystal (Persson et al., 1975). Investigation of isotropic restricted diffusion was performed with a sediment of fresh baker's yeast (trade name: Kronjäst from a local supermarket) prepared by dispersing yeast in tap water (1:1 volume ratio) in a glass vial, transferring with a syringe to a 10 mm NMR tube to a sample height of 40 mm, and keeping the tube in an upright position overnight at 4 ºC to allow the cells to settle under the force of gravity into a 20 mm high pellet (Malmborg et al., 2006).

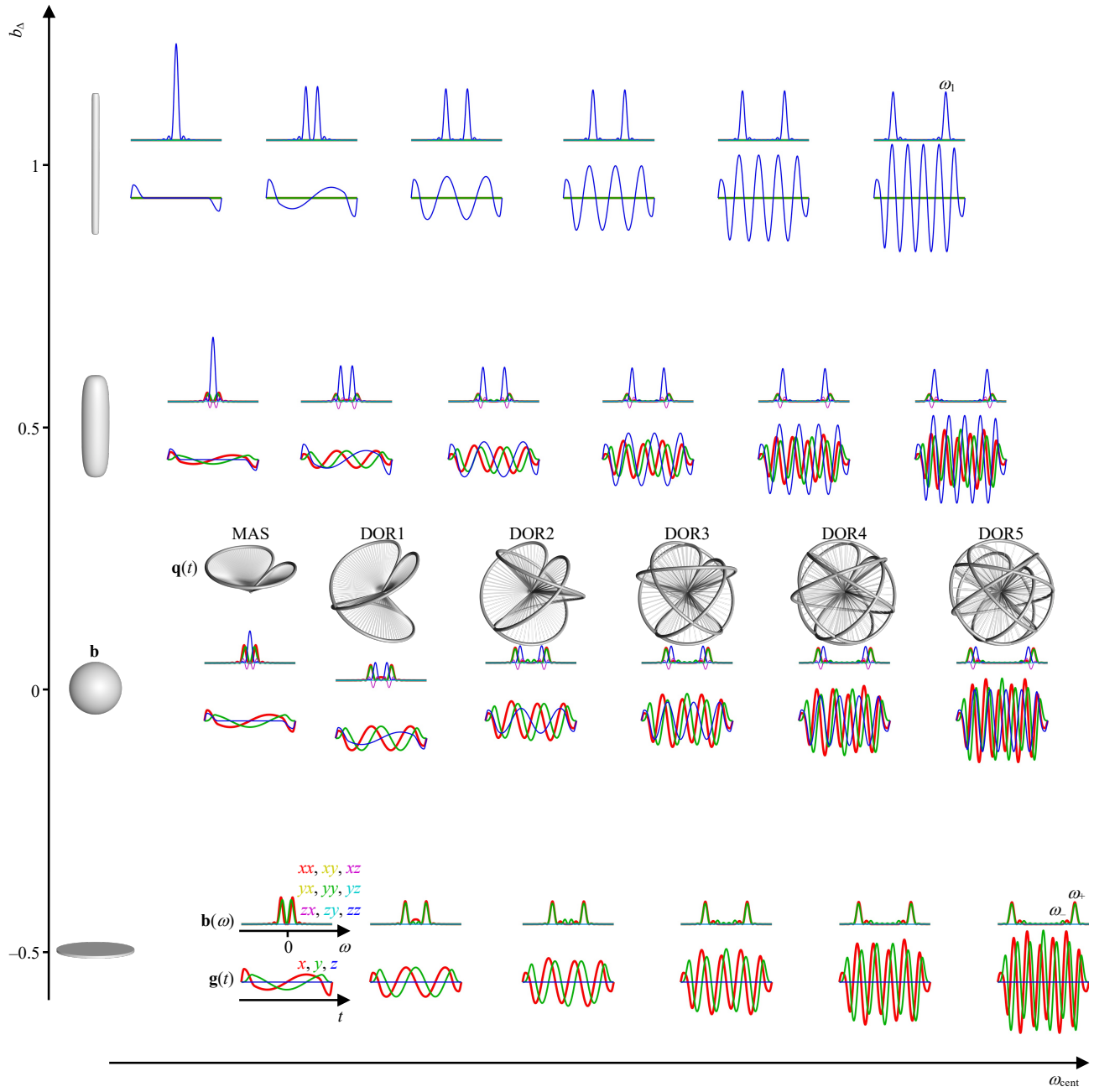

Figure 3. Gradient waveforms $\mathbf{g}(t)$ for comprehensive exploration of the 2D space of centroid frequency ω_{cent} and anisotropy b_Δ of the tensor-valued encoding spectrum $\mathbf{b}(\omega)$. Magic-angle spinning (MAS) and double rotation (DORn) with variable frequency ratio n give q-vector trajectories $\mathbf{q}(t)$ shown as 3D plots for the $b_\Delta = 0$ cases. The waveforms are generated according to the scheme in Figure 2 using $\varepsilon_{up} = 0.03\,\tau$, $\varepsilon_{down} = 0.12\,\tau$, $\Delta\psi_2 = 2\pi$, $b_\eta = 0$, and identical b-values for a 2D array of $n = 0, 1, \ldots, 5$ and $b_\Delta = –0.5, 0, 0.5$, and 1 with the angles $\zeta_1 = 0$ and $\zeta_2 = 54.7°$ for $n = 0$ and $\zeta_1 = 90°$ and $\zeta_2 = –54.7°$ for $n > 0$. Superquadric tensor glyphs (Kindlmann, 2004) along the vertical axis illustrate $\mathbf{b}$ for the chosen values b_Δ. The main maxima in $\mathbf{b}(\omega)$ are located at the frequencies ω_1 and ω_+ given in Eq. (57). Values of ω_{cent} and b_Δ, including non-idealities originating from the finite durations of the dephasing and rephasing lobes of $g_{1D}(t)$, are obtained by Eqs. (32) and (34) using numerically evaluated $\mathbf{b}(\omega)$ according to Eqs. (4), (18), and (22).

MRI was performed on a Bruker Avance-Neo 500 MHz spectrometer equipped with an 11.7 T vertical bore magnet and a MIC-5 microimaging probe fitted with a 10 mm RF insert for observation of ^{1}H. Images were acquired with a Topspin 4.0 implementation of a spin-echo prepared single-shot RARE sequence (available at https://github.com/daniel-topgaard/md-dmri) using 0.6×0.6 mm^2 resolution in a plane perpendicular to the tube axis, 1 mm slice thickness, and 16×16×1 matrix size. Diffusion encoding employed pairs of identical gradient waveforms bracketing the 180º pulse in the preparation block (Lasič et al., 2014). Data was acquired for 8 b-values up to $6.44\cdot10^9$ sm^{-2} and 15 orientations (Θ,Φ) for each of the 24 waveforms spanning the ω_{cent},b_Δ-plane in Figure 3 using maximum gradient amplitude 3 T/m and waveform duration $\tau = 25$ ms, giving values of ω_{cent} in the range from 20 to 260 Hz. With 5 s recycle delay, the total measurement time was approximately 4 h for each sample. The sample temperature was controlled with a Bruker VT unit to 278 K for the yeast and 291 K for the isotropic solutions and liquid crystal. For the yeast, the image slice was placed in the middle of the pellet and 10 mm below the bottom of the supernatant. Image reconstruction, definition of regions-of-interest, and curve fitting was performed in Matlab using in-house code available at https://github.com/daniel-topgaard/md-dmri (Nilsson et al., 2018).

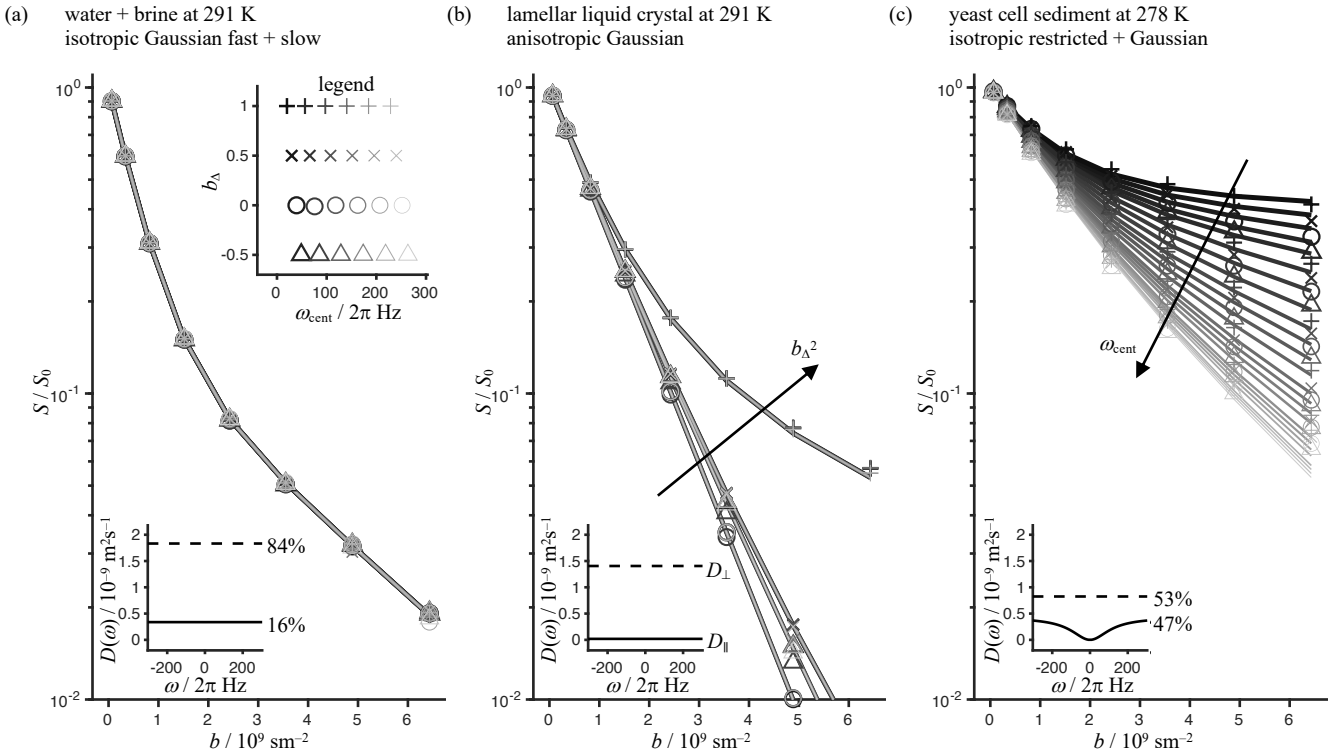

Figure 4. Experimental (markers) and fitted (lines) normalized powder-averaged signal S/S_0 vs. b-value for phantoms with well-defined diffusion properties. (**a**) Tube-in-tube assembly of pure water and a concentrated solution of magnesium nitrate in water ("brine") giving rise to two isotropic Gaussian (ω-independent) components. Two-component fit based on Eq. (41) gives diffusion spectra $D(\omega)$ as shown in the inset with percentages indicating the relative contributions. The legend shows the 24 investigated values in the ω_{cent} (gray scale) and b_Δ (marker style) space corresponding to the gradient waveforms in Figure 3 with duration $\tau = 25$ ms, maximum gradient strength 3 Tm^{-1}, and pairs of waveforms bracketing the 180º pulse in the spin-echo preparation. (**b**) Polydomain lamellar liquid crystal giving Gaussian parallel and perpendicular diffusivities, $D_\parallel$ and $D_\perp$, as estimated by a fit of Eq. (43). (**c**) Sediment of yeast cells with intra- and extracellular compartments, the former exhibiting restricted (ω-dependent) diffusion. The inset shows $D(\omega)$ resulting from a two-component fit with one spherically restricted (solid) and one Gaussian (dashed) component. For the former component, the signal was obtained by numerical integration of Eq. (39) with $D(\omega)$ given by Eq. (25) with $d = 3$ and D_∞ constrained to zero.

Figure 4 compiles experimental data and fits for all investigated samples. To facilitate visual inspection of the highly multidimensional data acquired as a function of (b,ω_{cent},b_Δ,Θ,Φ), the signal data was averaged over b-tensor orientations (Θ,Φ)

and displayed as conventional Stejskal-Tanner plots of $\log_{10}(S)$-vs.-b with the ω_{cent},b_Δ-dimensions coded into marker grayscale and style. For the isotropic Gaussian sample in Figure 4a, all data points collapse onto a single master curve, thereby verifying that all 24 waveforms spanning the ω_{cent},b_Δ-plane in Figure 3 indeed give the same b-value. The pronounced non-linearity of the $\log_{10}(S)$-vs.-b plot indicates the presence of multiple species with different diffusivities, and the bi-exponential fit yields diffusivities consistent with pure water (fast) and water in the saturated magnesium nitrate solution (slow). The anisotropic Gaussian phantom Figure 4b yields data points stratified into one master curve for each of the four values of b_Δ, verifying independence of ω_{cent}. The data is well fitted by the expression for randomly oriented axisymmetric diffusion tensors in Eq. (43), giving estimates of the diffusivities $D_\parallel$ and $D_\perp$ parallel and perpendicular to the cylindrical symmetry axis of the crystallites. The observations $D_\parallel << D_\perp$ and $D_\parallel \approx 0$ are consistent with diffusion in a lamellar liquid crystal with planar surfactant bilayers being nearly impermeable to water (Callaghan and Söderman, 1983). For the isotropic restriction phantom in Figure 4c, the signal depends strongly on ω_{cent} as expected. In this case there is no clear stratification of data points into separate master curves on account of the interplay between b_Δ and ω_{cent} as reported in the legend in Figure 4a and explained in detail below Eq. (57). The minor dependence of ω_{cent} on b_Δ is admittedly a drawback of our current approach for generating waveforms, which we however believe is justified by the simplicity and transparency of the mathematical expressions in Eqs. (49)-(57). The sum of isotropic restricted and Gaussian components, given by Eqs. (41) and (39), yields an excellent fit to the acquired data, showing that the data features no dependence on the value of b_Δ. To account for the fact that $b(\omega)$ for in particular the $b_\Delta = 0$ waveforms cannot be well approximated with a delta-function at a single value of ω, the signal for the restricted component was obtained by numerical evaluation of the integral in Eq. (39) using the diffusion spectrum $D(\omega)$ for spherical compartments in Eq. (25). The obtained diffusivities are consistent with previous results for intra- and extracellular water in yeast cell sediments (Åslund and Topgaard, 2009). Taken together, the data in Figure 4 verifies that the set of waveforms allow detailed exploration of the 2D ω_{cent},b_Δ-plane of multidimensional diffusion encoding.

5 Conclusions and outlook

The proposed family of double-rotation gradient waveforms enables comprehensive sampling of both the frequency and "shape" dimensions of diffusion encoding as required for detailed characterization of restriction and anisotropy in heterogeneous materials such as brain tissues. The present waveforms, deriving from simple geometrical considerations and generated by compact mathematical expressions, are suitable for pre-clinical investigations of tissue samples or small animals on high-gradient systems. By numerical optimizations to maximize the b-value for given gradient strength (Topgaard, 2013; Sjölund et al., 2015), mitigating image artifacts from eddy currents (Yang and McNab, 2019) and concomitant gradients (Szczepankiewicz et al., 2019), and further minimizing side-lobes in the encoding spectra (Hennel et al., 2020), we anticipate that the waveforms may be adapted for human *in vivo* studies. The merging of oscillating gradients (Aggarwal, 2020) and tensor-valued encoding (Reymbaut, 2020) into a common acquisition protocol encourages further development of a joint analysis framework, for instance by augmenting current nonparametric diffusion tensor distributions (Topgaard, 2019b) with a Lorentzian frequency dimension (Narvaez et al., 2021; Narvaez et al., 2022) or building on the concept of confinement tensors (Yolcu et al., 2016; Boito et al., 2022).

Author contributions

DT conceived the project. HJ, LS, and DT developed theory and software. HJ acquired data. HJ and DT processed and analyzed data. HJ, LS, and DT wrote the manuscript.

Acknowledgements

This work was financially supported the Swedish Foundation for Strategic Research (ITM17-0267), Swedish Research Council (2018-03697, 2022-04422_VR), and Chinese Scholarship Council.

References

Aggarwal, M.: Restricted diffusion and spectral content of the gradient waveforms, In: Topgaard, D. (Ed.), Advanced Diffusion Encoding Methods in MRI, Royal Society of Chemistry, Cambridge, UK, pp. 103-122, doi: 10.1039/9781788019910-00103, 2020.

Andrew, E. R., Bradbury, A., Eades, R. G.: Removal of dipolar broadening of nuclear magnetic resonance spectra of solids by specimen rotation, Nature, 183, 1802-1803, doi: 10.1038/1831802a0, 1959.

Arbabi, A., Kai, J., Khan, A. R., Baron, C. A.: Diffusion dispersion imaging: Mapping oscillating gradient spin-echo frequency dependence in the human brain, Magn Reson Med, 83, 2197-2208, doi: 10.1002/mrm.28083, 2020.

Åslund, I., Topgaard, D.: Determination of the self-diffusion coefficient of intracellular water using PGSE NMR with variable gradient pulse length, J. Magn. Reson., 201, 250-254, doi: 10.1016/j.jmr.2009.09.006, 2009.

Balinov, B., Jönsson, B., Linse, P., Söderman, O.: The NMR self-diffusion method applied to restricted diffusion. Simulation of echo attenuation from molecules in spheres and between planes, J. Magn. Reson. A, 104, 17-25, doi: 10.1006/jmra.1993.1184, 1993.

Basser, P. J., Mattiello, J., Le Bihan, D.: Estimation of the effective self-diffusion *tensor* from the NMR spin echo, J. Magn. Reson. B, 103, 247-254, doi: 10.1006/jmrb.1994.1037, 1994.

Boito, D., Yolcu, C., Özarslan, E.: Multidimensional diffusion MRI methods with confined subdomains, Front. Phys., 10, 830274, doi: 10.3389/fphy.2022.830274, 2022.

Boss, B. D., Stejskal, E. O.: Anisotropic diffusion in hydrated vermiculite, J. Chem. Phys., 43, 1068-1069, doi: 10.1063/1.1696823, 1965.

Callaghan, P. T.: Translational dynamics & magnetic resonance. Oxford University Press, Oxford, 2011.

Callaghan, P. T., Manz, B.: Velocity exchange spectroscopy, J. Magn. Reson. A, 106, 260-265, doi: 10.1006/jmra.1994.1036, 1994.

Callaghan, P. T., Söderman, O.: Examination of the lamellar phase of Aerosol OT/water using pulsed field gradient nuclear magnetic resonance, J. Phys. Chem., 87, 1737-1744, doi: 10.1021/j100233a019, 1983.

Callaghan, P. T., Stepišnik, J.: Frequency-domain analysis of spin motion using modulated-gradient NMR, J. Magn. Reson. A, 117, 118-122, doi: 10.1006/jmra.1995.9959, 1995.

Caprihan, A., Fukushima, E.: Flow measurements by NMR, Phys. Rep., 198, 195-235, doi: 10.1016/0370-1573(90)90046-5, 1990.

Carr, H. Y., Purcell, E. M.: Effects of diffusion on free precession in nuclear magnetic resonance experiments, Phys. Rev., 94, 630-638, doi: 10.1103/PhysRev.94.630, 1954.

Cory, D. G., Garroway, A. N., Miller, J. B.: Applications of spin transport as a probe of local geometry, Polymer Prepr., 31, 149-150, doi: 1990.

Daimiel Naranjo, I., Reymbaut, A., Brynolfsson, P., Lo Gullo, R., Bryskhe, K., Topgaard, D., Giri, D. D., Reiner, J. S., Thakur, S., Pinker-Domenig, K.: Multidimensional diffusion magnetic resonance imaging for characterization of tissue microstructure in breast cancer patients: A prospective pilot study, Cancers, 13, 1606, doi: 10.3390/cancers13071606, 2021.

de Almeida Martins, J. P., Topgaard, D.: Two-dimensional correlation of isotropic and directional diffusion using NMR, Phys. Rev. Lett., 116, 087601, doi: 10.1103/PhysRevLett.116.087601, 2016.

de Swiet, T. M., Mitra, P. P.: Possible systematic errors in single-shot measurements of the trace of the diffusion tensor, J. Magn. Reson. B, 111, 15-22, doi: 10.1006/jmrb.1996.0055, 1996.

Douglass, D. C., McCall, D. W.: Diffusion in paraffin hydrocarbons, J. Phys. Chem., 62, 1102-1107, doi: 10.1021/j150567a020, 1958.

Eriksson, S., Lasič, S., Nilsson, M., Westin, C.-F., Topgaard, D.: NMR diffusion encoding with axial symmetry and variable anisotropy: Distinguishing between prolate and oblate microscopic diffusion tensors with unknown orientation distribution, J. Chem. Phys., 142, 104201, doi: 10.1063/1.4913502, 2015.

Eriksson, S., Lasič, S., Topgaard, D.: Isotropic diffusion weighting by magic-angle spinning of the *q*-vector in PGSE NMR, J. Magn. Reson., 226, 13-18, doi: 10.1016/j.jmr.2012.10.015, 2013.

Frydman, L., Chingas, G. C., Lee, Y. K., Grandinetti, P. J., Eastman, M. A., Barrall, G. A., Pines, A.: Variable-angle correlation spectroscopy in solid-state nuclear magnetic resonance, J. Chem. Phys., 97, 4800-4808, doi: 10.1063/1.463860, 1992.

Haeberlen, U.: High resolution NMR in solids. Selective averaging. Academic Press, New York, 1976.

Hahn, E. L.: Spin echoes, Phys. Rev., 80, 580-594, doi: 10.1103/PhysRev.80.580, 1950.
Hennel, F., Michael, E. S., Pruessmann, K. P.: Improved gradient waveforms for oscillating gradient spin-echo (OGSE) diffusion tensor imaging, NMR Biomed, e4434, doi: 10.1002/nbm.4434, 2020.
Kärger, J.: Zur Bestimmung der Diffusion in einem Zweibereichsystem mit Hilfe von gepulsten Feldgradienten, Ann. Phys., 479, 1-4, doi: 10.1002/andp.19694790102, 1969.
Kindlmann, G.: Superquadric tensor glyphs, In: Deussen, O., Hansen, C., Keim, D.A., Saupe, D. (Eds.), Proceedings IEEE TVCG/EG Symposium on Visualization, Eurographics Association Aire-la-Ville, Switzerland, pp. 147-154, doi: 10.2312/VisSym/VisSym04/147-154, 2004.
Kingsley, P. B.: Introduction to diffusion tensor imaging mathematics: Part II. Anisotropy, diffusion-weighting factors, and gradient encoding schemes, Conc. Magn. Reson. A, 28A, 123-154, doi: 10.1002/cmr.a.20049, 2006.
Lasič, S., Åslund, I., Topgaard, D.: Spectral characterization of diffusion with chemical shift resolution: Highly concentrated water-in-oil emulsion, J. Magn. Reson., 199, 166-172, doi: 10.1016/j.jmr.2009.04.014, 2009.
Lasič, S., Stepišnik, J., Mohoric, A.: Displacement power spectrum measurements by CPMG in constant gradient, J. Magn. Reson., 182, 208-214, doi: 2006.
Lasič, S., Szczepankiewicz, F., Eriksson, S., Nilsson, M., Topgaard, D.: Microanisotropy imaging: quantification of microscopic diffusion anisotropy and orientational order parameter by diffusion MRI with magic-angle spinning of the *q*-vector, Front. Physics, 2, 11, doi: 10.3389/fphy.2014.00011, 2014.
Le Bihan, D., Breton, E., Lallemand, D., Grenier, P., Cabanis, E., Laval-Jeantet, M.: MR imaging of intravoxel incoherent motions - application to diffusion and perfusion in neurological disorders, Radiology, 161, 401-407, doi: 10.1148/radiology.161.2.3763909, 1986.
Lundell, H., Lasič, S.: Diffusion encoding with general gradient waveforms, In: Topgaard, D. (Ed.), Advanced Diffusion Encoding Methods in MRI, Royal Society of Chemistry, Cambridge, UK, pp. 12-67, doi: 10.1039/9781788019910-00012, 2020.
Lundell, H., Nilsson, M., Dyrby, T. B., Parker, G. J. M., Cristinacce, P. L. H., Zhou, F. L., Topgaard, D., Lasič, S.: Multidimensional diffusion MRI with spectrally modulated gradients reveals unprecedented microstructural detail, Sci. Rep., 9, 9026, doi: 10.1038/s41598-019-45235-7, 2019.
Lundell, H., Sønderby, C. K., Dyrby, T. B.: Diffusion weighted imaging with circularly polarized oscillating gradients, Magn. Reson. Med., 73, 1171-1176, doi: 10.1002/mrm.25211, 2015.
Malmborg, C., Sjöbeck, M., Brockstedt, S., Englund, E., Söderman, O., Topgaard, D.: Mapping the intracellular fraction of water by varying the gradient pulse length in *q*-space diffusion MRI, J. Magn. Reson., 180, 280-285, doi: 10.1016/j.jmr.2006.03.005, 2006.
Mills, R.: Self-diffusion in normal and heavy water in the range 1-45°, J. Phys. Chem., 77, 685-688, doi: 10.1021/j100624a025, 1973.
Mori, S., van Zijl, P. C. M.: Diffusion weighting by the trace of the diffusion tensor within a single scan, Magn. Reson. Med., 33, 41-52, doi: 10.1002/mrm.1910330107, 1995.
Narvaez, O., Svenningsson, L., Yon, M., Sierra, A., Topgaard, D.: Massively multidimensional diffusion-relaxation correlation MRI, Front. Phys., 9, 793966, doi: 10.3389/fphy.2021.793966, 2022.
Narvaez, O., Yon, M., Jiang, H., Bernin, D., Forssell-Aronsson, E., Sierra, A., Topgaard, D.: Model-free approach to the interpretation of restricted and anisotropic self-diffusion in magnetic resonance of biological tissues, arXiv:2111.07827, doi: 10.48550/arXiv.2111.07827, 2021.
Neuman, C. H.: Spin echo of spins diffusing in a bounded medium, J. Chem. Phys., 60, 4508-4511, doi: 10.1063/1.1680931, 1974.
Nielsen, J. S., Dyrby, T. B., Lundell, H.: Magnetic resonance temporal diffusion tensor spectroscopy of disordered anisotropic tissue, Sci. Rep., 8, 2930, doi: 10.1038/s41598-018-19475-y, 2018.
Nilsson, M., Szczepankiewicz, F., Lampinen, B., Ahlgren, A., de Almeida Martins, J. P., Lasič, S., Westin, C.-F., Topgaard, D.: An open-source framework for analysis of multidimensional diffusion MRI data implemented in MATLAB, Proc. Intl. Soc. Mag. Reson. Med., 26, 5355, doi: 2018.
Parsons, E. C., Does, M. D., Gore, J. C.: Modified oscillating gradient pulses for direct sampling of the diffusion spectrum suitable for imaging sequences, Magn. Reson. Imaging, 21, 279-285, doi: 10.1016/s0730-725x(03)00155-3, 2003.

Persson, N.-O., Fontell, K., Lindman, B., Tiddy, G. J. T.: Mesophase structure studies by deuteron magnetic resonance observations for the sodium octanoate-decanol-water system, J. Colloid Interface Sci., 53, 461-466, doi: 10.1016/0021-9797(75)90063-6, 1975.

Price, W. S.: NMR studies of translational motion. Cambridge University Press, Cambridge, 2009.

Reymbaut, A.: Diffusion anisotropy and tensor-valued encoding, In: Topgaard, D. (Ed.), Advanced Diffusion Encoding Methods in MRI, Royal Society of Chemistry, Cambridge, UK, pp. 68-102, doi: 10.1039/9781788019910-00068, 2020.

Reymbaut, A., Zheng, Y., Li, S., Sun, W., Xu, H., Daimiel Naranjo, I., Thakur, S., Pinker-Domenig, K., Rajan, S., Vanugopal, V. K., Mahajan, V., Mahajan, H., Critchley, J., Durighel, G., Sughrue, M., Bryskhe, K., Topgaard, D.: Clinical research with advanced diffusion encoding methods in MRI, In: Topgaard, D. (Ed.), Advanced Diffusion Encoding Methods in MRI, Royal Society of Chemistry, Cambridge, UK, pp. 406-429, doi: 10.1039/9781788019910-00406, 2020.

Samoson, A., Lippmaa, E., Pines, A.: High resolution solid-state NMR: Averaging of second-order effects by means of a double-rotor, Mol. Phys., 65, 1013-1018, doi: 10.1080/00268978800101571, 1998.

Sjölund, J., Szczepankiewicz, F., Nilsson, M., Topgaard, D., Westin, C.-F., Knutsson, H.: Constrained optimization of gradient waveforms for generalized diffusion encoding, J. Magn. Reson., 261, 157-168, doi: 10.1016/j.jmr.2015.10.012, 2015.

Stejskal, E. O., Tanner, J. E.: Spin diffusion measurements: Spin echoes in the presence of a time-dependent field gradient, J. Chem. Phys., 42, 288-292, doi: 10.1063/1.1695690, 1965.

Stepišnik, J.: Analysis of NMR self-diffusion measurements by a density matrix calculation, Physica B, 104, 305-364, doi: 10.1016/0378-4363(81)90182-0, 1981.

Stepišnik, J.: Time-dependent self-diffusion by NMR spin-echo, Physica B, 183, 343-350, doi: 10.1016/0921-4526(93)90124-O, 1993.

Stepišnik, J.: Validity limits of Gaussian approximation in cumulant expansion for diffusion attenuation of spin echo, Physica B, 270, 110-117, doi: 10.1016/S0921-4526(99)00160-X, 1999.

Stepišnik, J., Callaghan, P. T.: The long time tail of molecular velocity correlation in a confined fluid: observation by modulated gradient spin-echo NMR, Physica B, 292, 296-301, doi: 10.1016/S0921-4526(00)00469-5, 2000.

Szczepankiewicz, F., Westin, C. F., Nilsson, M.: Maxwell-compensated design of asymmetric gradient waveforms for tensor-valued diffusion encoding, Magn. Reson. Med., 82, 1424-1437, doi: 10.1002/mrm.27828, 2019.

Tanner, J. E.: Self diffusion of water in frog muscle, Biophys. J., 28, 107-116, doi: 10.1016/S0006-3495(79)85162-0, 1979.

Topgaard, D.: Isotropic diffusion weighting in PGSE NMR: Numerical optimization of the *q*-MAS PGSE sequence, Microporous Mesoporous Mater., 178, 60-63, doi: 10.1016/j.micromeso.2013.03.009, 2013.

Topgaard, D.: Director orientations in lyotropic liquid crystals: Diffusion MRI mapping of the Saupe order tensor, Phys. Chem. Chem. Phys., 18, 8545-8553, doi: 10.1039/c5cp07251d, 2016.

Topgaard, D.: Multidimensional diffusion MRI, J. Magn. Reson., 275, 98-113, doi: 10.1016/j.jmr.2016.12.007, 2017.

Topgaard, D.: Multiple dimensions for random walks, J. Magn. Reson., 306, 150-154, doi: 10.1016/j.jmr.2019.07.024, 2019a.

Topgaard, D.: Diffusion tensor distribution imaging, NMR Biomed., 32, e4066, doi: 10.1002/nbm.4066, 2019b.

Wadsö, L., Anderberg, A., Åslund, I., Söderman, O.: An improved method to validate the relative humidity generation in sorption balances, Eur. J. Pharm. Biopharm., 72, 99-104, doi: 10.1016/j.ejpb.2008.10.013, 2009.

Woessner, D. E.: N.M.R. spin-echo self-diffusion measurements on fluids undergoing restricted diffusion, J. Phys. Chem., 67, 1365-1367, doi: 10.1021/j100800a509, 1963.

Xu, J., Jiang, X., Devan, S. P., Arlinghaus, L. R., McKinley, E. T., Xie, J., Zu, Z., Wang, Q., Chakravarthy, A. B., Wang, Y., Gore, J. C.: MRI-cytometry: Mapping nonparametric cell size distributions using diffusion MRI, Magn. Reson. Med., 85, 748-761, doi: 10.1002/mrm.28454, 2021.

Yang, G., McNab, J. A.: Eddy current nulled constrained optimization of isotropic diffusion encoding gradient waveforms, Magn. Reson. Med., 81, 1818-1832, doi: 10.1002/mrm.27539, 2019.

Yolcu, C., Memic, M., Simsek, K., Westin, C. F., Özarslan, E.: NMR signal for particles diffusing under potentials: From path integrals and numerical methods to a model of diffusion anisotropy, Phys. Rev. E, 93, 052602, doi: 10.1103/PhysRevE.93.052602, 2016.